Materials Science Forum
ISSN: 1662-9752, Vol. 1186, pp 59-72
doi:10.4028/p-ir99uX

Submitted: 2026-01-20
Revised: 2026-02-17
Accepted: 2026-02-26
Online: 2026-04-16

Process Optimization for Forging an AA6082 Automotive Upper Control Arm

Liju Zhou[1,a], Leigang Wang[1,b], Mingxiao Shi[2,c], Angela Daniela La Rosa[3,d], Elisabete F. Reia da Costa[4,e] and Xiang Ma[4,f*]

[1]School of Materials Science and Engineering, Jiangsu University, 212013 Zhenjiang, China

[2]School of Materials Science and Engineering, Jiangsu University of Science and Technology, 212003 Zhenjiang, China

[3]Department of Manufacturing and Civil Engineering, Norwegian University of Science and Technology, 2815 Gjøvik, Norway

[4]SINTEF Industry, POB 124 Blindern, 0314 Oslo, Norway

[a]ljzhou9907@163.com, [b]lgwang@mail.ujs.edu.cn, [c]smx@just.edu.cn, [d]angela.d.l.rosa@ntnu.no, [e]elisabete.f.r.costa@sintef.no, [f*]xiang.ma@sintef.no

Keywords: 6082 aluminum alloy, automotive control arm, rolling, forging, die design, finite element analysis, response surface methodology.

Abstract. This study examines the forging process of an aluminum upper control arm for automotive applications. To address the geometric complexity and forming challenges, a multi-step forging route is developed, consisting of roll forging, two-stage bending, pre-forging and final forging. Finite element analysis (FEA) using DEFORM-3D software is employed to optimize key forming process parameters in the pre-forging stage. The response surface methodology (RSM), combined with the Box–Behnken design, is utilized to construct predictive models and identify optimal parameter combinations. A successful forged upper control arm is subsequently produced using these optimized forming parameters. The findings demonstrate that integrating FEA with statistical process optimization strengthens the predictive accuracy of the process design and supports defect-free forging of AA6082 upper control arms.

Introduction

The control arm (including upper and lower arms) is one of the most critical components in a vehicle's chassis suspension system, responsible for both guiding and transmitting loads. It transfers various forces and moments acting on the wheels through the suspension system to the vehicle's frame or body, thereby ensuring stable and safe driving performance. Given the complex service conditions, control arms must exhibit high strength, stiffness, impact toughness and fatigue resistance [1]. With the growing emphasis on lightweight technologies, there has been increasing research and industrial interest in replacing steel with aluminum alloys for control arm manufacturing [2]. Among various forming methods, forging stands out for its ability to produce components with superior mechanical properties. In particular, 6082 aluminum alloy (AA6082), an Al-Mg-Si series alloy, has emerged as one of the most preferred alloys for forged control arms due to its high specific strength, excellent hot workability and strong corrosion resistance [3-5].

Compared with steel, aluminum alloys show several distinct forging characteristics: (1) a narrow deformation temperature window [6-7]; (2) pronounced strain-rate sensitivity. Numerous studies on the hot-deformation behavior of aluminum alloys show strain rate sensitivity [8-10]. Thus, forging equipment with a faster and steadier working speed should be selected, for example, a mechanical press; and (3) a strong tendency to adhere to die surfaces [11-12]. In terms of heat treatment, wrought aluminum alloys typically undergo annealing (including homogenization annealing, recrystallization annealing, and stress-relief annealing), retrogression treatment, quenching (or solution treatment), and aging. Specially, Al–Mg–Si series alloys exhibit a pronounced delayed-aging (stagnation) effect: after quenching, the material inevitably experiences a period of natural room-temperature holding before artificial aging, during which premature clustering reduces the subsequent age-hardening

response [13]. The forging trial in this work reduces the interval between quenching and artificial aging to retain the hardenability of the 6082 alloy. It is noted that the complex geometry of control arm component, combined with the narrow forging temperature range and intricate flow behavior of aluminum alloys, may pose significant challenges. If the forming process is not properly designed, various defects may occur in the forged parts. Hot forming process analysis and shape control are achieved primarily through finite element (FE) simulation [14-16].

In this study, by integrating deformation theory with FE modelling, a comprehensive forging strategy is developed. FE software, DEFORM-3D, is employed to optimize key forming process parameters, aiming to enhance the quality and reliability of the forged component. Particularly, the response surface methodology [17] and the Box–Behnken design approach [18] are used to assist in optimizing the pre-forging stage. Trial forging is conducted based on the simulated results.

SSbD (Safe and Sustainable by Design) Guided Analysis of Forming Process

The *SSbD* principle used in [19] is closely followed in analyzing and designing the forming process. The forging geometry of the upper control-arm examined in this study is shown in Fig. 1. The component has an overall *U*-shaped geometry. Except for the two nearly cylindrical bushing-boss ends, the remaining sections form an asymmetric I-shaped cross-section perpendicular to the bending axis. The central web is thin, and the ribs along the arm edges include geometrically complex features, such as protruding mounting ears.

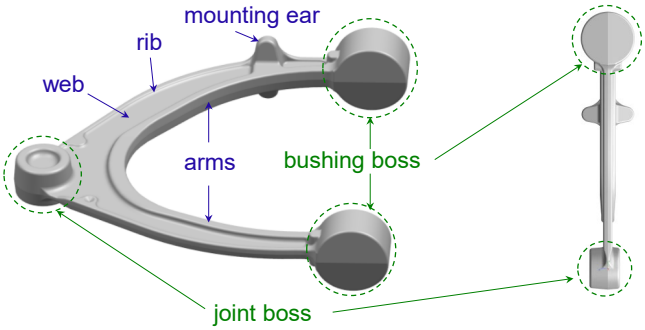

(a) Front view (b) Side view

Fig. 1. The geometry of the upper control arm.

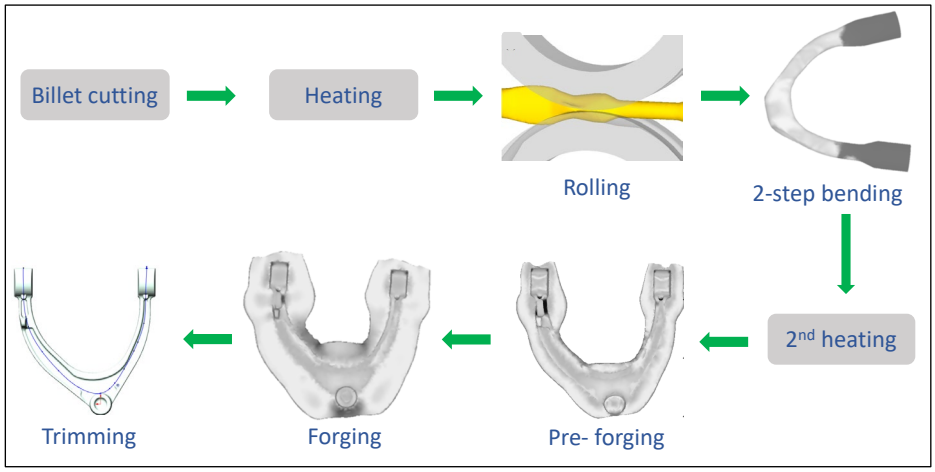

Fig. 2. Process flow chart of the control arm forming.

A structural analysis of the forging reveals key challenges associated with its forming process:

(1). The significant variation in cross-section along the bending axis requires precise control of material flow during forming.

(2). The large regions located at the two bushing bosses, the protruding mounting ears, and the ball joint boss area pose a risk of incomplete die filling.

(3). During the formation of the I-shaped cross-section, the component is particularly susceptible to the development of folding defects, which may compromise structural integrity.

The control arm forging is a bent, long-axis forging. To enhance material utilization and ensure the required forging quality, a multi-stage forming route is necessary to transform the initially simple bar billet into the final component geometry. Accordingly, a process scheme comprising billet preparation, pre-forging, and final forging is proposed. The billet-preparation stage consists of roll-forging followed by bending. The forging process flow is illustrated in Fig. 2. Especially, roll forging is employed to facilitate the redistribution of billet volume along its longitudinal axis, thereby significantly enhancing material utilization during the billet-preparation stage. The control arm exhibits localized geometric complexity, and direct single-step forging after billet preparation would likely cause folding, incomplete die filling, or excessive deformation. To mitigate these issues, an intermediate pre-forging operation is introduced between billet preparation and the final forging stage. Similar multi-step forming strategy on long shaft forgings is employed in [20].

The FE Model

The FE model is created by first constructing the billet and die geometries for each forming stage using *SolidWorks*, after which the models are exported in STL format and imported into DEFORM-3D for simulation. Key process parameters for roll forging and bending are assigned based on established production experience (Table 1). To accurately represent the thermo-mechanical evolution occurring in actual manufacturing, the final billet geometry obtained at the end of each forming step is used directly as the initial geometry for the subsequent step in the FE analysis.

Table 1. The process parameter setting in FE simulation of roll forging and bending.

Process step	Process parameter	Value
Roll forging	Billet temperature (°C)	490
	Die temperature (°C)	200
	Rolling speed (r/min)	50
Bending	Die temperature (°C)	20
	Forming speed (mm/s)	100

Because deformation in the roll-forging and bending stages is modest, the billet mesh is limited to approximately 60,000 elements to improve computational efficiency. A volume-compensation procedure is also applied. In contrast, the pre-forging stage involves more complex material flow and larger local deformation gradients; therefore, the mesh is refined to 160,000 elements with a mesh size ratio of 5 to ensure adequate resolution of the deformation field. Mesh-convergence behavior is also examined by comparing results obtained from two mesh levels: the current mesh, and a mesh with element size increased by roughly one-third. Both solutions converge while the current mesh setting shows a slight improvement. Proper remeshing is applied during the forming process.

The constitutive model of AA6082 is chosen from the material database of DEFORM-3D. A shear friction model, which is widely adopted for bulk metal forming simulations, is employed throughout the analysis [21]. To account for billet bite-in during roll forging, a higher friction factor of 0.7 is specified at the roll entry surface, while a value of 0.4 is used for bending operation. Thermal boundary conditions are also included. The interfacial thermal contact conductivity between billet and dies is set to 1100 W/(m^2·K), and the convective heat-transfer coefficient between the billet surface and the surrounding air is set to 20 W/(m^2·K).

FE Results of Roll-Forging and Bending

The details of the simulated roll forging and bending can be found in [22]. The optimized roll-forging die design is performed by FEM. The FE results indicate that increasing the initial billet temperature leads to reductions in both the maximum equivalent stress and the peak forming load, with an optimal initial temperature range of $T_p \geq 470$ °C. Variations in die temperature exert only a

minor influence on the overall billet temperature; however, higher die temperatures noticeably reduce the thermal gradient between the billet surface and core. Increasing the roll-forging speed results in higher maximum equivalent stress and forming load, while also causing a significant increase in the minimum billet temperature during processing. Favorable formability is achieved when the friction factor lies within the range 0.4–0.55 for roll-forging only. The simulation results demonstrate that employing a two-pass roll-forging sequence followed by two-station bending produces a preform that closely approximates the desired pre-forged geometry, with uniform stress distribution and a favorable metal flow pattern. This helps establish a robust foundation for the subsequent pre-forging and final-forging stages of the control-arm manufacturing process.

Optimization of Control Arm Pre-Forging Process Parameters Based on RSM

RSM design

The RS design in this study is developed using the Design-Expert software package. Among the various design methodologies available in the software, the Box–Behnken Design (BBD) and the Central Composite Design are the most widely employed. BBD is particularly suitable for systems involving two to five factors, where each factor is restricted to three discrete levels, making it advantageous for response-surface modeling scenarios in which the parameter ranges are relatively moderate. For these reasons, the BBD methodology is selected for the present study.

The die load during the pre-forging stage (Y_1) and the average maximum equivalent stress (Y_2) are chosen as the primary response outputs. Four process parameters are selected as design variables: billet temperature (X_1), die preheating temperature (X_2), upper-die velocity (X_3), and the friction factor at the die–billet interface (X_4). A four-factor, three-level BBD scheme is generated in Design-Expert, and the selected levels for each design variable are summarized in Table 2. As recommended in [23], the billet preheating temperature range for AA6082 is chosen as 450-490 °C: a narrow range with an upper limit of 490 °C to avoid approaching the melting point. The die preheating temperature range (200-300 °C), around 200 °C lower than the billet temperature, follows the recommendation in [23] for a closed die forging using mechanical press. A 2500-ton mechanical press is used, and the forging velocity is set within the medium-to-high range (50–150 mm/s) to limit billet cooling and reduce die contact time [24]. The friction factor range of 0.2-0.4 is chosen as low and medium friction occurs between die and material [25].

Table 2. Design variables and level setting.

Variable	No.	Level range		
billet preheating temperature (°C)	X_1	450	470	490
die preheating temperature (°C)	X_2	200	250	300
upper-die velocity (mm·s^{-1})	X_3	50	100	150
friction factor	X_4	0.2	0.3	0.4

Simulation models are constructed sequentially according to the design scheme, and the simulation outputs are shown in Table 3.

Table 3. The test and results of BBD.

No.	X_1 (℃)	X_2 (℃)	X_3 (mm/s)	X_4	Y_1 (kN)	Y_2 (MPa)
1	470	200	50	0.3	6895	71.51
2	470	250	150	0.2	6306	75.94
3	470	250	100	0.3	6982	73.27
4	470	300	100	0.4	7001	73.86
5	470	250	100	0.3	6982	73.27
6	470	300	100	0.2	5903	71.48
7	450	250	150	0.3	7133	77.46
8	490	300	100	0.3	6179	68.39
9	470	250	50	0.2	6216	69.67
10	450	200	100	0.3	7273	75.48
11	470	250	100	0.3	6982	73.27
12	450	300	100	0.3	7347	75.08
13	450	250	50	0.3	7532	72.93
14	450	250	100	0.4	7782	74.11
15	470	200	100	0.4	7090	73.01
16	470	300	150	0.3	6470	75.80
17	470	250	100	0.3	6982	73.27
18	490	250	150	0.3	6593	73.66
19	470	250	100	0.3	6982	73.27
20	470	250	150	0.4	7373	75.56
21	470	200	100	0.2	6161	73.80
22	490	250	100	0.4	6949	69.48
23	470	200	150	0.3	6901	75.19
24	490	250	100	0.2	5848	71.57
25	490	250	50	0.3	6410	67.40
26	490	200	100	0.3	6391	71.10
27	470	300	50	0.3	6789	67.21
28	470	250	50	0.4	7115	68.04
29	450	250	100	0.2	6853	75.14

Establishment and verification of the RS model

The RS model approximates the relationship between the response value and design variables using polynomial expressions. A second-order polynomial is selected because forging responses exhibit nonlinear behavior and variable interactions, and this is the highest order fully supported by RSM theory. Thus, the real response value Y is described as:

$$Y = \beta_0 + \sum_{i=1}^{k} \beta_i X_i + \sum_{i=1}^{k} \beta_i X_i^2 + \sum_{i \neq j} \beta_{ij} X_i X_j + \varepsilon \quad (1)$$

Where: β_0, β_I, β_j, β_{ij}: polynomial coefficients; X_i, X_j: design variables; ε: the approximation error of the objective function.

Least-squares regression is applied using Design-Expert software to fit the relationships between the design variables and the responses. The polynomial expressions of Y_1 and Y_2 are given as:

$$Y_1 = 24345.653 - 82.393X_1 + 75.198X_2 - 59.479X_3 + 3214.012X_4 - 0.0717X_1X_2 + 0.1466X_1X_3 + 21.529X_1X_4 - 0.033X_2X_3 + 8.451X_2X_4 + 8.413X_3X_4 + 0.006X_1^2 - 0.085X_2^2 - 0.018X_3^2 - 18778X_4^2 \quad (2)$$

$$Y_2 = 86.53203 - 0.022164X_1 - 0.161708X_2 - 0.283564X_3 - 13.6701X_4 - 0.000579X_1X_2 + 0.000433X_1X_3 - 0.132921X_1X_4 + 0.000491X_2X_3 + 0.158372X_2X_4 + 0.062578X_3X_4 \quad (3)$$

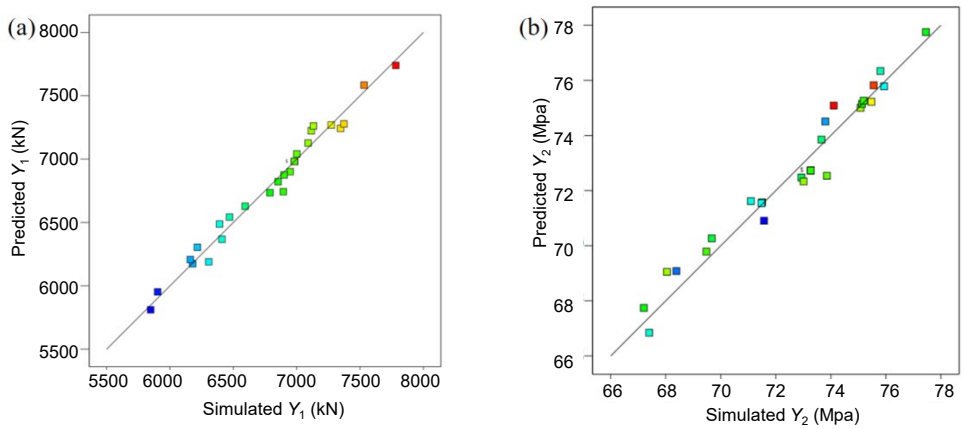

Fig. 3. Comparison between predicted and simulated values Y_1 (a) and Y_2 (b).

To ensure the model's reliability, predicted values by Eqs (2) and (3) are plotted in Fig. 3 against the corresponding simulated values in Table 3. The 45° line in Fig. 3 represents zero-error conditions, while the color gradient (blue for early runs and red for later runs) indicates the sequence of simulation cases. The predicted values align closely with the simulated results, with most points lying near the zero-error line indicating high predictive accuracy.

To assess the reliability of the experimental results and the credibility of the mathematical models, significance testing is performed. Common analytical approaches include analysis of variance (ANOVA) and coefficient-of-determination–based evaluations. ANOVA is applied in this work to evaluate the statistical significance of the regression model and to determine the sensitivity and relative importance of each process parameter, rather than overall model reliability. The ANOVA results for the die load and the average maximum equivalent stress are summarized in Table 4 and Table 5, respectively. The *F*-value reflects the degree of influence exerted by each factor on the corresponding response: a larger first-order *F*-value indicates a stronger effect. The *P*-value signifies the statistical significance of the model: values of $P < 0.01$ (denoted by **) indicate a highly significant effect, values in the range $0.01 \leq P < 0.05$ (denoted by *) indicate a significant effect, and $P \geq 0.05$ suggests limited significance, with increased model error.

Table 4. Analysis of variance of pre-forging forming load.

Source	Sum of Squares	df	Mean Square	*F*-value	*P*-value	
Model	6.33×10^{12}	14.00	4.52×10^{11}	48.49	< 0.0001	**
X_1	2.57×10^{12}	1.00	2.57×10^{12}	275.45	<0.0001	
X_2	8.69×10^{10}	1.00	8.69×10^{10}	9.32	0.01	
X_3	2.76×10^{9}	1.00	2.766×10^{9}	0.30	0.60	
X_4	3.02×10^{12}	1.00	3.02×10^{12}	324.52	< 0.0001	
X_1X_2	2.05×10^{10}	1.00	2.05×10^{10}	2.20	0.16	
X_1X_3	8.48×10^{10}	1.00	8.48×10^{10}	9.10	0.01	
X_1X_4	7.426×10^{9}	1.00	7.426×10^{9}	0.80	0.39	
X_2X_3	2.64×10^{10}	1.00	2.64×10^{10}	2.84	0.11	
X_2X_4	7.146×10^{9}	1.00	7.146×10^{9}	0.77	0.40	
X_3X_4	7.086×10^{9}	1.00	7.086×10^{9}	0.76	0.40	
X_1^2	3.716×10^{9}	1.00	3.716×10^{9}	0.40	0.54	
X_2^2	2.93×10^{11}	1.00	2.93×10^{11}	31.45	< 0.0001	
X_3^2	1.35×10^{10}	1.00	1.35×10^{10}	1.45	0.25	
X_4^2	2.29×10^{11}	1.00	2.29×10^{11}	24.55	0.00	
Residual	1.30×10^{11}	14.00	9.326×10^{9}			
Lack of fit	1.30×10^{11}	10.00	1.30×10^{10}			
Cor total	6.46×10^{12}	28.00				

Table 5. Variance analysis of the average maximum effective stress.

Source	Sum of Squares	df	Mean Square	*F*-value	*P*-value	
Model	199.4	10	19.94	39.16	<0.0001	**
X_1	68.15	1	68.15	133.85	<0.0001	
X_2	5.7	1	5.7	11.19	0.0036	
X_3	113.21	1	113.21	222.34	<0.0001	
X_4	1.05	1	1.05	2.05	0.169	
X_1X_2	1.34	1	1.34	2.63	0.122	
X_1X_3	0.7497	1	0.7497	1.47	0.2407	
X_1X_4	0.2827	1	0.2827	0.5552	0.4658	
X_2X_3	6.03	1	6.03	11.84	0.0029	
X_2X_4	2.51	1	2.51	4.93	0.0395	
X_3X_4	0.3916	1	0.3916	0.7691	0.392	
Residual	9.16	18	0.5092			
Lack of fit	9.16	14	0.6546			
Cor total	208.57	28				

As shown in Table 4, the regression model for the pre-forging die load exhibits a *P*-value < 0.0001, demonstrating a highly significant influence and indicating strong agreement between the design variables and the response. Thus, the response-surface model provides sufficient fidelity for subsequent optimization. A comparison of *F*-values reveals that the relative influence of the design variables on the pre-forging load, from greatest to least, is: friction factor, billet temperature, die preheating temperature, and upper-die velocity.

The overall reliability and goodness-of-fit of the response surface models is assessed using the coefficient of determination (R^2) and the adjusted coefficient of determination R_{adj}^2. R^2 assumes a value within the range [0, 1]. Values approaching unity indicate a high degree of agreement between the model predictions and the observed results. Similarly, R_{adj}^2 also lies within [0, 1] and accounts for the number of model terms; values closer to 1 signify strong predictive capability and minimal deviation between the predicted and actual responses. As summarized in Table 6, the two response-surface models explain 97.98% and 95.61% of the variance in their respective responses, demonstrating excellent model fidelity and confirming that the proposed regression models provide an accurate representation of the experimental trends.

Table 6. Error analysis of regression equations.

Fitting variable	R^2	R_{adj}^2
Y_1	0.9798	0.9596
Y_2	0.9561	0.9316

Analysis of influencing factors in the RS model

Fig. 4 illustrates the response surfaces describing the effects of two-factor interactions among the four process variables (billet temperature (X_1), die-preheating temperature (X_2), upper-die velocity (X_3), and friction factor (X_4)) on the pre-forging die load (Y_1).

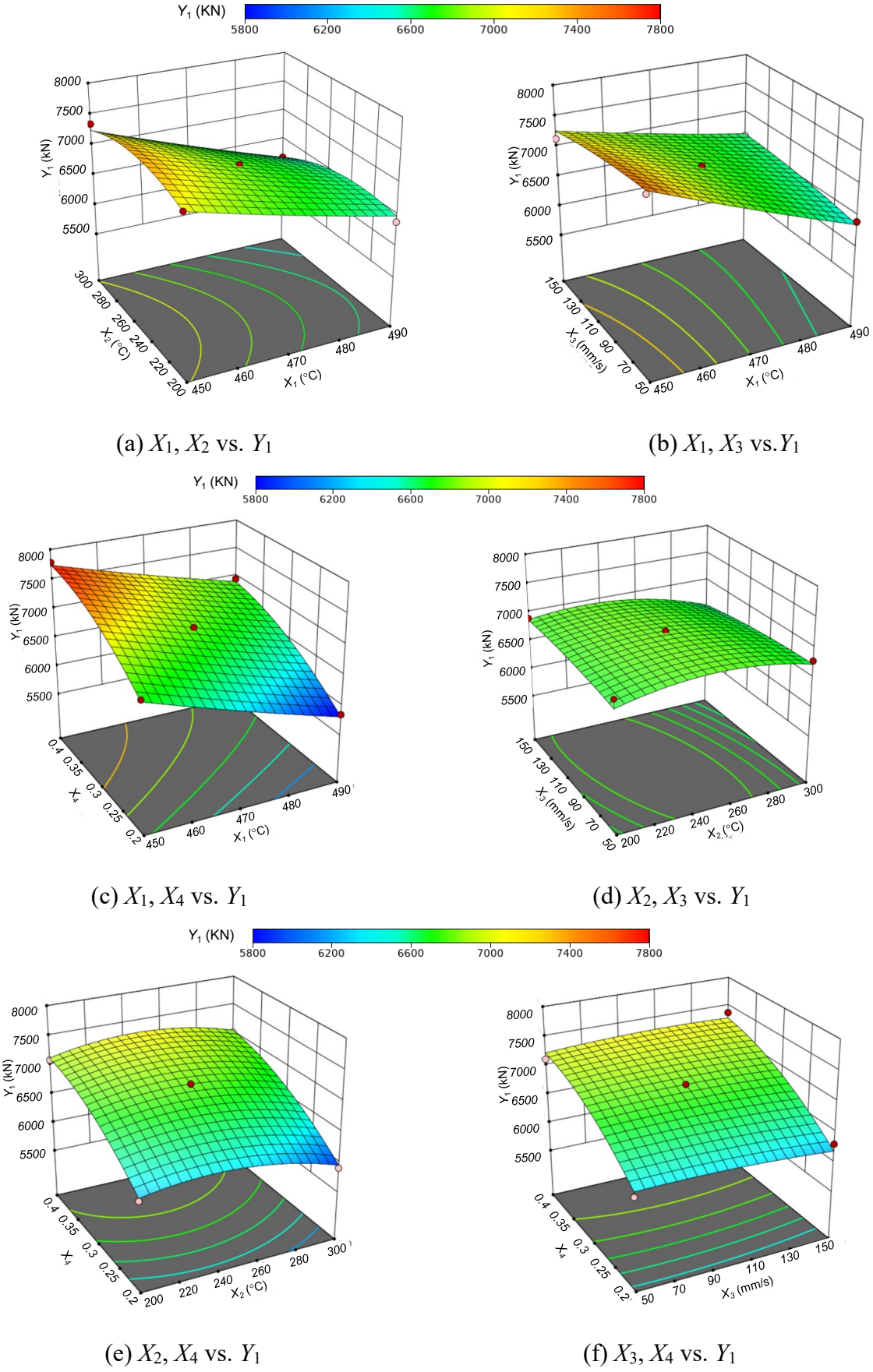

(a) X_1, X_2 vs. Y_1

(b) X_1, X_3 vs.Y_1

(c) X_1, X_4 vs. Y_1

(d) X_2, X_3 vs. Y_1

(e) X_2, X_4 vs. Y_1

(f) X_3, X_4 vs. Y_1

Fig. 4. Response surface of different influencing factors on pre-forging die load.

The response surfaces in Fig. 4 reveal that the influence of different two-factor interactions on the pre-forging die load varies considerably. The interaction between billet temperature and die-preheating temperature shows that increasing billet temperature consistently reduces the die load, with the effect becoming more pronounced when die-preheating temperature is elevated (Fig. 4(a)). When billet temperature interacts with upper-die velocity, billet temperature again dominates the load response, whereas changes in die velocity produce only secondary effects (Fig. 4(b)). A much stronger interaction effect is observed between billet temperature and friction factor (Fig. 4(c)), where the die load changes sharply with friction level, especially at lower billet temperatures, highlighting friction as one of the most influential process variables. Interactions involving die-preheating temperature, whether paired with billet temperature, upper-die velocity, or friction factor (Fig. 4 (a), (d), (e)), show moderate but consistent effects on die load, reinforcing its role as a secondary factor. Moreover, variations in upper-die velocity produce the smallest changes in die load across all interaction surfaces (Fig. 4 (b), (d), (f)), indicating limited sensitivity to this parameter compared with temperature or friction.

The combined trends in Fig. 4 demonstrate that the dominant factors affecting pre-forging die load are the friction factor and billet temperature, followed by die-preheating temperature, while upper-die velocity has the weakest influence.

The response surfaces in Fig. 5 show that the average maximum equivalent stress Y_2 is jointly influenced by billet and die-preheating temperatures, upper-die velocity, and friction factor, with varying degrees of sensitivity. Higher billet temperature and die preheating temperature reduce the thermal gradients and maintain the billet at elevated temperature enhancing material flow (Fig. 5 (a), (e)). The interaction between billet temperature and upper-die velocity indicates that lower die-closing speeds lead to lower stress, particularly at higher billet temperatures (Fig. 5 (b)). Friction factor plays only a minor role when billet temperature is low, but improved lubrication (lower friction factor) further reduces peak stress at elevated temperatures or in combination with high die-preheating temperature (Fig. 5 (c), (e), (f)). Interactions involving die-preheating temperature and upper-die velocity produce only modest stress variations, confirming their secondary influence (Fig. 5 (d)).

The analysis indicates that upper-die velocity has the strongest effect on the equivalent stress, followed by billet temperature and die-preheating temperature, whereas the friction factor exerts only a limited influence on this response.

The optimization module in Design-Expert is employed to evaluate the fitted polynomial response-surface models. In this study, the optimization objective is to minimize both the pre-forging die load and the average maximum equivalent stress, thereby identifying the optimal combination of process parameters. The optimization is restricted to the prescribed parameter ranges to ensure the validity of the solution.

Using this approach, Design-Expert recommends the following optimal parameter set: a billet temperature of 490 °C, a die-preheating temperature of 300 °C, an upper-die velocity of 50 mm/s, and a friction factor of 0.26.

Numerical simulations performed using this optimized parameter combination are compared with the predictions and the results are summarized in Table 7. The deviation between the predicted and simulated values of the pre-forging load is 1.98%, while the error for the average maximum equivalent stress is only 0.04%. These small deviations demonstrate that the optimized response-surface model provides a reliable and accurate prediction of both die load and maximum equivalent stress during the pre-forging process.

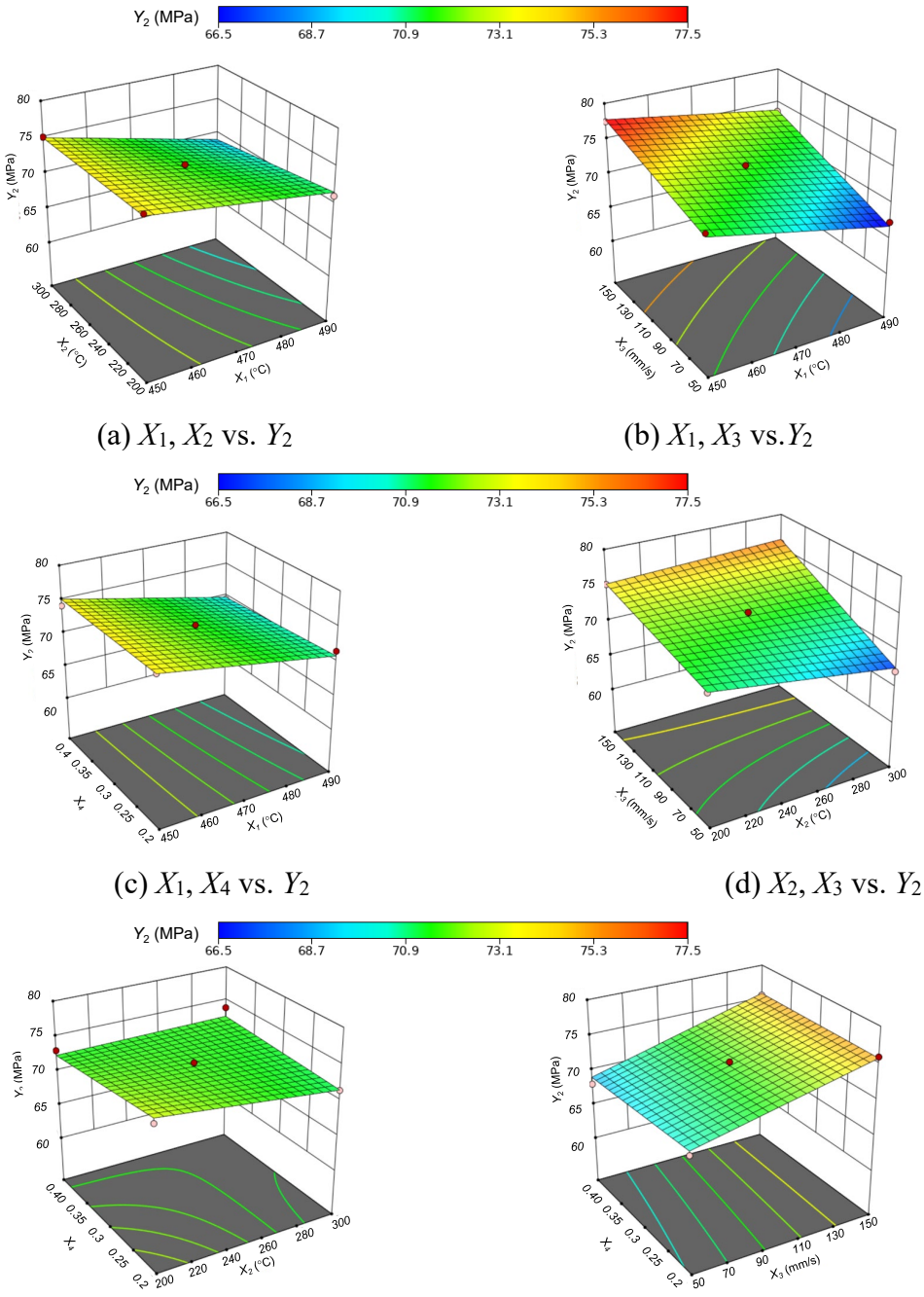

(a) X_1, X_2 vs. Y_2 (b) X_1, X_3 vs.Y_2

(c) X_1, X_4 vs. Y_2 (d) X_2, X_3 vs. Y_2

(e) X_2, X_4 vs. Y_2 (f) X_3, X_4 vs. Y_2

Fig. 5. Response surface of influencing factors on the average maximum effective stress of pre-forging.

Table 7. Predicted and simulated values for the optimization of process parameters.

X_1 (°C)	X_2 (°C)	X_3 (mm/s)	X_4	Prediction		Simulation	
				Y_1 (kN)	Y_2 (MPa)	Y_1 (kN)	Y_2 (MPa)
490	300	50	0.26	5843	64.41	5961	64.38

Simulated results of the pre-forging process

Based on the optimized pre-forging process parameters described above, a thermo-mechanical coupled analysis is conducted for the pre-forging under the optimal conditions. Fig. 6 shows the equivalent-stress distribution during deformation, with the main volume region names marked in Fig. 6(c) and (d). As the upper die descends, the large material volumes at the bushing bosses and joint boss contact the lower die first and begin to fill the cavity (Fig. 6(a)), producing noticeably higher equivalent stress than the still-free regions. During this early stage, the forming load increases slowly

(Fig. 7). When the arm sections subsequently contact the die (Fig. 6(b)), deformation intensifies and the load begins to rise more noticeably. As the die continues to close, the cavity becomes mostly filled. Only the deeper regions, such as the bushing-boss pockets, joint-boss area, mounting-ear zones, and the inner ribs, remain partially unfilled at this stage (Fig. 6(c)). Excess material is then pushed toward the flash through the flash-bridge region, where the smallest height produces the highest equivalent stress and greatest flow resistance, helping ensure complete die filling. Once flash forms and restricts metal flow, the forming load rises rapidly. At die closure, the billet fully fills the cavity and exhibits a relatively uniform stress distribution without excessive local concentration (Fig. 6(d)). By the end of pre-forging, the die load reaches 5961 kN and cavity filling is satisfactory.

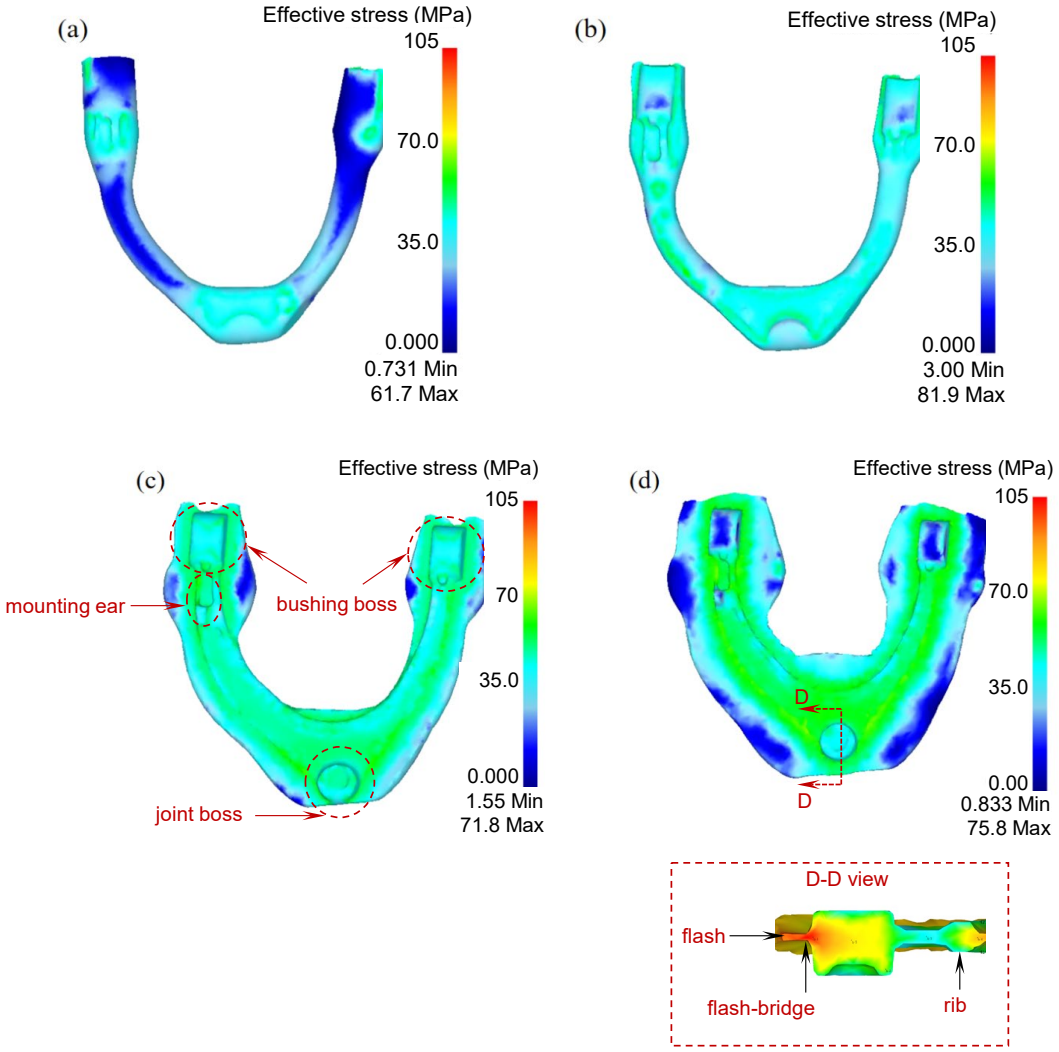

Fig. 6. Evolution of effective stress distributions during pre-forging process.

Fig. 8 shows that maximum equivalent stress from the simulated pre-forging process stays near or below the average value of 64 MPa in the early and middle stages, then rises in the later stage. Under the optimized parameters, it remains below 105 MPa, indicating stable and uniform deformation.

Although this work focuses on pre-forging, the final forging step is also simulated with the same process parameter setup. These forming process parameters are implemented in practice and a successful forged upper control arm is produced (Fig. 9). Key geometric features, such as the central axial distance between the joint boss and the bushing boss, are measured and compared with the simulation results, showing a deviation of 3%. This confirms that the simulation accurately predicts the final forging outcome.

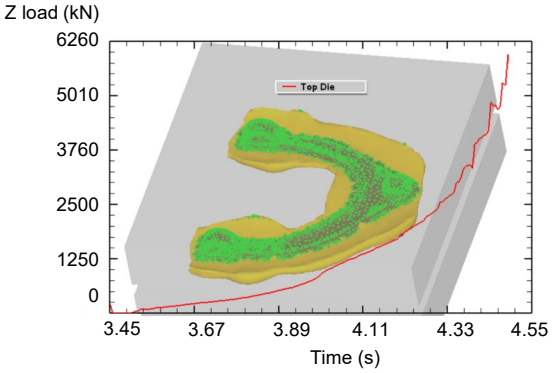

Fig. 7. Pre-forging load-time curves.

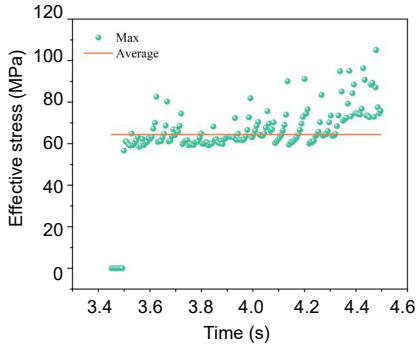

Fig. 8. Scatter plot of maximum effective stress in simulated pre-forging process.

Fig. 9. Forged upper control arm.

The material model used in this study is the default DEFORM-3D library model and does not include microstructural parameters. The constitutive model and microstructural parameters of 6082 aluminum alloy can be obtained through physical experiments in future work. This would improve the accuracy of the simulations and enable analysis and control of the forging process from both macroscopic and microscopic perspectives.

Due to limitations in design capability, a two-stage free-bending process is adopted in the current bending stage. In the future, new dies may be developed to achieve one-step bending, thereby improving forging efficiency. In addition, the control-arm forging examined in this work exhibits relatively large flash. Exploring more optimized billet-preparation processes may help improve material utilization.

Conclusion

This work examines the pre-forging process of an aluminum alloy upper control arm for automotive applications. FE simulation is combined with the response surface methodology to optimize key forming process parameters in the pre-forging stage. The main findings are summarized as follows:

(1) The pre-forging die load and the average maximum equivalent stress are used as the primary optimization objectives. Four key process parameters (billet temperature, die-preheating temperature, upper-die velocity, and friction factor) are designated as design variables, and a Box–Behnken Design framework is constructed to develop the response surface models.

(2) The accuracy and statistical significance of the BBD models are verified, and the individual effects of each design variable on the objectives are analyzed. A multi-objective optimization is subsequently performed, identifying the following optimal parameter combination: billet temperature of 490 °C, die-preheating temperature of 300 °C, upper-die velocity of 50 mm/s, and friction factor of 0.26.

(3) A thermo-mechanical coupled FE analysis is conducted using the optimized process parameters to evaluate the pre-forging behavior. FE simulation yields a pre-forging load of 5961 kN and an average maximum equivalent stress of 64.4 MPa. The results show stable forming behavior, with controlled metal flow and adequate cavity filling. A successful forged upper control arm is subsequently produced using these optimized forming parameters.

Acknowledgement

This work is partially supported by the National Natural Science Foundation of China (Grant No. 51775249), SFI Future Aluminium Structures (FAST) funded by the Research Council of Norway (Grant No. 360119), the COGNIMAN project (Grant Agreement No. 101058477) funded by the Horizon Europe research and innovation program of the European Union, and the POLYKAP project funded by SINTEF SEP program.

References

[1] X. Zou, Y. Zhou, Y. Xiao, D. Yuan, G. Xiang, Research on fatigue life of all-terrain vehicle control arm based on measured load spectrum, Cobot, 1:16, 2022.

[2] J. Hirsch, Recent development in aluminium for automotive applications, Transactions of Nonferrous Metals Society of China, 24(7):1995-2002, 2014.

[3] X. Qian, N. Parson, X. Chen, Effects of Mn addition and related Mn-containing dispersoids on the hot deformation behavior of 6082 aluminum alloys, Materials Science and Engineering A, 764: 138253, 2019.

[4] L. Deng, H. Zhang, G. Li, X. Tang, P. Yi, Z. Liu, X. Wang, J. Jin, Processing map and hot deformation behavior of squeeze cast 6082 aluminum alloy, Transactions of Nonferrous Metals Society of China, 32(7): 2150-2163, 2022.

[5] Schindler, P. Kawulok, V. Očenášek, P. Opěla, R. Kawulok, S. Rusz, Flow stress and hot deformation activation energy of 6082 aluminium alloy influenced by initial structural state, Metals, 9(12): 1248, 2019.

[6] L. Zhou, J. Luo, Y. Xiang, Effect of initial forging temperature on mechanical properties of free forging 6061 aluminum alloy (in Chinese), Hot Working Technology, (13): 109-111, 2020.

[7] E. Gokcil, S. Akdi, Y. Birol, A novel processing route for the manufacture of EN AW 6082 forged components, Materials Research Innovations, 19:311-314, 2015.

[8] D. Feng, X. Zhang, S. Liu, Z. Wu, Q. Tan, Rate controlling mechanisms in hot deformation of 7A55 aluminum alloy, Transactions of Nonferrous Metals Society of China, 24(1): 28-35, 2014.

[9] X. Yuan, W. Rui, X. Guo, Research on hot deformation behaviors of 6061 Al alloy. Materials Science Forum, 1032: 141-146, 2021.

[10] L. Wang, Z. Tao, Y. Huang, M. Shi, K. Tang, X. Ma, Recovering and hot deformation processing of recycled spray formed 7055 aluminum alloy powders, K. Mocellin, P.O. Bouchard, R. Bigot, T. Balan (eds), Proceedings of the 14th International Conference on the Technology of Plasticity - Current Trends in the Technology of Plasticity (ICTP 2023), 4:586-597, Lecture Notes in Mechanical Engineering, Springer, Cham, 2024.

[11] F. Widerøe, T. Welo, Conditions for sticking friction between aluminium alloy AA6060 and tool steel in hot forming, Key Engineering Materials, 491:121-128, 2011.

[12] J. Pujante, M. Vilaseca, D. Casellas, et al., The role of adhesive forces and mechanical interaction on material transfer in hot forming of aluminium, Tribology Letters, 59:10, 2015.

[13] J. Kim, E. Kobayashi, T. Sato, Influence of natural aging time on two-step aging behavior of Al-Mg-Si(-Cu) alloys, Materials Transactions, 56(11): 1771-1780, 2005.

[14] R.T. Prabhu, Modelling studies on effects of deformation speed, preform shape, and upset ratio on the forging characteristics of the aerospace structural Al alloys, International Journal of Materials and Product Technology, 54(4):291-305, 2017.

[15] P.F. Gao, M.Y. Fei, X.G. Yan, et al., Prediction of the folding defect in die forging: A versatile approach for three typical types of folding defects, Journal of Manufacturing Processes, 39:181-191, 2019.

[16] H. Hu, X. Qin, D. Zhang, X. Ma, A novel severe plastic deformation method for manufacturing AZ31 magnesium alloy tube, The International Journal of Advanced Manufacturing Technology, 98(1-4): 897-903, 2018.

[17] G. Box, K. Wilson, On the experimental attainment of optimum conditions. Journal of the Royal Statistical Society Series B, 13(1):1-45, 1951.

[18] G. Box, D. Behnken, Some new three-level designs for the study of quantitative variables, Technometrics. 2(4):455–75, 1960.

[19] R. Rajagopal, et al., Optimizing the implementation of safe and sustainable by design to better enable sustainable innovation, iScience, 28(8): 113116, 2025.

[20] L. Deng, J. Xia, X. Wang, Precision forging technology for long shaft parts, In: Precision Forging Technology and Equipment for Aluminum Alloy, Springer Series in Advanced Manufacturing, Springer, Singapore, 2022.

[21] Y. Huang, L. Wang, M. Shi, X. Ma, A contact and friction model for forming of galvanized steel sheet based on fractal theory, G. Daehn, J. Cao, B. Kinsey, E. Tekkaya, A. Vivek, Y. Yoshida (eds), Proceedings of the 13th International Conference on the Technology of Plasticity - Forming the Future (ICTP2021), 97-112, The Minerals, Metals & Materials Series, Springer, Cham, 2021.

[22] L. Zhou, R. Sun, Z. Gao, D. Si, L. Wang, Forging process on automotive aluminum alloy control arm based on CAE, Forging & Stamping Technology, 49(3):1-7, 2024.

[23] G. Kuhlman, Forging of Aluminum Alloys, S. Semiatin (eds), ASM Handbook, 14A: 299-312, ASM International, 2005.

[24] L. Deng, J. Xia, X. Wang, Precision forging presses for aluminum alloy, In: Precision Forging Technology and Equipment for Aluminum Alloy, Springer Series in Advanced Manufacturing, Springer, Singapore, 2022.

[25] Y. Hwang, C. Lu, G. Lin, et al., Die design and finite-element analysis for the hot forging of automotive wheel frames made of aluminium alloy, The International Journal of Advanced Manufacturing Technology, 137, 2681–2695, 2025.